ADVANCED OPTICAL MATERIALS
www.advopticalmat.de

Check for updates

Giant Nonlinear Optical Response in Triple Cation Halide Mixed Perovskite Films

*Hamad Syed, Wenchi Kong, Venkatesh Mottamchetty, Kwang Jin Lee, Weili Yu, Venugopal Rao Soma, Jianjun Yang, and Chunlei Guo**

The versatility of perovskites through chemical composition modification is critical for enhancing performance of a range of potential applications such as light emitters and integrated photovoltaics. However, a systematic study on the nonlinear optical (NLO) responses of these perovskites is still lacking. Here, for the first time, the NLO properties of triple cation mixed halide perovskite (TCMHP) films, $(Cs_{0.06}FA_{0.79}MA_{0.15})Pb(I_{0.85}Br_{0.15})_3$, using Z-scan and time-resolved spectroscopy, are investigated. It is found that TCMHP film shows strong saturable absorption at 395 nm, reverse saturable absorption such as two- and three-photon absorption (2PA, 3PA) at 790 nm (near the bandgap), and 3PA at 1200 nm. The 3PA phenomena at 790 nm are attributed to the phonon-assisted anti-Stokes process. The 2PA and 3PA coefficients are estimated to be ≈2.1 cm MW^{-1} and ≈900 cm^3 GW^{-2}, respectively, which are an order of magnitude larger than those of $MAPbI_3$ and other perovskites. Moreover, it is demonstrated that these giant 2PA and 3PA coefficients of TCMHP can be used to realize optical stabilization. The observed strong multiphoton absorption response will enable TCMHP materials to be suitable for various nonlinear optical applications such as multiphoton-based imaging, optical modulator, and all-optical switching devices.

1. Introduction

Organometal halide perovskites have received a great amount of attention owing to their simplicity in fabrication, low cost, and exceptional properties including high photostability, extremely long charge diffusion length, and thermal stability. The perovskites have become emerging high-performance materials for various optoelectronic applications such as solar cells,[1–3] light emitting diodes,[4,5] photodetectors,[6,7] and lasers.[8,9]

The halide perovskites also exhibit strong nonlinear optical (NLO) responses, thus opening up possibilities for optoelectronic device applications.[10–14] For instance, organic–inorganic hybrid perovskites with large two- and three-photon absorption (2PA, 3PA) properties[14–16] can be utilized in applications such as bioimaging,[17,18] optical limiting,[19] optical sensor protection,[20] and optical data storage.[21]

Nonlinear absorption properties of single crystal, nanocrystal, and filmed perovskites have been intensively studied.[10–16,22–24] Recently, lead halide perovskites such as $MAPbI_3$ ($MA = CH_3NH_3$) and $MAPbBr_3$ have shown higher multiphoton absorption (MPA) probability as the excitation wavelength increases in the IR region.[10–14,22–24] Johnson et al.[25] reported that the observation of third-order nonlinearities and decay kinetics in $MAPbBr_3$ and $MAPbBr_2I$ with different halogen composition. They showed that the third-order nonlinearities of these materials are larger than those of conventional semiconductors. The photoluminescence of $MAPbBr_3$ single crystal has also been observed in the green region (522–550 nm) with 1044 nm femtosecond laser excitation due to 2PA.[26] Similar nonlinear optical properties were reported in inorganic perovskites, including $CsPbI_3$ and $CsPbBr_3$.[22,27,28]

Another type of perovskite, formamidinium lead iodide ($FAPbI_3$), has a low bandgap (1.47 eV) and greater photostability and thermal stability[29,30] than $MAPbI_3$. However, $FAPbI_3$ has a weak structural stability due to humidity, which prevents it from real-life applications.[31] Recently, it has been demonstrated that the mixture of Cs and $MAPbI_3$, $CsMAPbI_3$, can lead to a stable solar cell with power conversion efficiency of ≈8%.[32] In addition, the mixture of Cs in $FAPbI_3$, such as $FA_{0.9}Cs_{0.1}PbI_3$, showed an improved thermal stability and results in high power conversion efficiency of ≈16.5%.[33] By using this material, Yi et al. have demonstrated power conversion efficiency up to 18% with a halide mixer I/Br.[34] The malleable association

Dr. H. Syed, W. Kong, Dr. V. Mottamchetty, Dr. W. Yu, Prof. J. Yang, Prof. C. Guo
The Guo China–US Photonics Laboratory
State Key Laboratory of Applied Optics
Changchun Institute of Optics
Fine Mechanics and Physics
Chinese Academy of Sciences
Changchun 130033, China
E-mail: guo@optics.rochester.edu
Dr. K. J. Lee, Prof. C. Guo
The Institute of Optics
University of Rochester
Rochester, NY 14627, USA
Prof. V. R. Soma
Advanced Center for Research in High Energy Materials (ACRHEM)
University of Hyderabad
Hyderabad 500046, Telangana, India
The ORCID identification number(s) for the author(s) of this article can be found under https://doi.org/10.1002/adom.201901766.

DOI: 10.1002/adom.201901766

 © 2020 WILEY-VCH Verlag GmbH & Co. KGaA, Weinheim

of cations (MA and FA) and halides (I and Br) along with hole transport materials, not only enhance the solar cell efficiency (>20.2%) but also improve the environmental stability compare to pure cation perovskites.[35]

The efficiency of photovoltaic devices can be further improved by triple cation mixed halide perovskites (TCMHPs). These materials show further improved thermal stability, less susceptible to moisture, and high fabrication tolerance, which yield a high power conversion efficiency up to ≈21%.[36] Recently, $(Cs_{0.06}FA_{0.79}MA_{0.15})Pb(I_{0.85}Br_{0.15})_3$ has been established as luminescent constituents owing to their broadband absorption. Interestingly, it has been found that photoluminescence quantum efficiency can be enhanced by increasing the excitation intensity due to the trap states filled with electrons.[37,38] Therefore, TCMHPs have emerged as versatile materials for development of a range of optoelectronic devices.

More recently, NLO properties of double cation mixed perovskite films[39] and halide mixed nanocrystals[40] have been studied. The nonlinear responses of these materials can enable a great amount of photonic applications. However, the NLO properties of TCMHP films have not been investigated yet. In this study, we systematically investigated the NLO properties of $(Cs_{0.06}FA_{0.79}MA_{0.15})Pb(I_{0.85}Br_{0.15})_3$ film by carrying out Z-scan measurements using femtosecond laser pulses. We observed a strong saturable absorption (SA) at 395 nm and reverse saturable absorptions (RSAs) at 790 and 1200 nm due to 2PA and 3PA. More importantly, we obtained a giant 3PA coefficient at 790 nm, which are even larger than those of organometal halide perovskites. We also revealed that the phonon-assisted anti-Stokes process enables 3PA at 790 nm.

2. Results and Discussions

The synthesis of TCMHP, $(Cs_{0.06}FA_{0.79}MA_{0.15})Pb(I_{0.85}Br_{0.15})_3$, is described in the Supporting Information and the Experimental Section. We prepared 500 nm thick TCMHP films by spin-coating on glass substrate and annealed at 100 °C for 1 h. **Figure 1**a displays the scanning electronic microscopic (SEM) image and inset shows its magnified image. The surface morphology confirms the evolution of micro-/nanosized grains and the mean size of micro-/nanosized grains is ≈500 nm.

Figure 1b depicts the X-ray diffraction (XRD) spectrum of annealed TCMHP film, standard TCMHP (nonannealed), and δ-phase $FAPbI_3$ and PbI_2 along with their crystal planes. The XRD peak at 14.2° and seven more peaks with their respective crystal planes confirm the intrinsic phase of perovskite as previously reported.[37] Two extremely small peaks observed at 11.7° and 12.5° correspond to nonperovskite δ-phase $FAPbI_3$ and PbI_2, respectively, [36] which would not affect the optical properties of the perovskite. In Figure 1c, UV–vis absorption spectrum shows strong absorption in the range of visible to near IR. Absorption onset around 780 nm, corresponding the energy bandgap, is shorter than pure α-phase $FAPbI_3$ (840 nm)

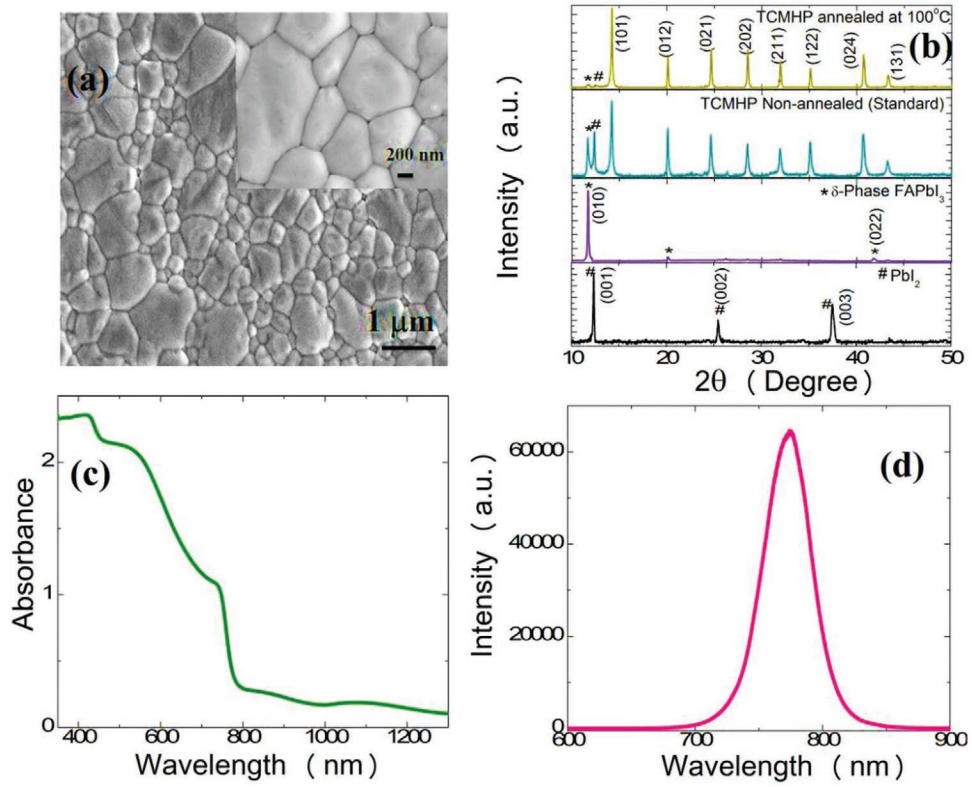

Figure 1. Basic morphology and optical characterizations of annealed $(Cs_{0.06}FA_{0.79}MA_{0.15})Pb(I_{0.85}Br_{0.15})_3$ (TCMHP) film. a) SEM image (inset: magnification image), b) XRD spectra of annealed TCMHP, standard TCMHP (nonannealed), δ-phase $FAPbI_3$ and PbI_2 along with their crystal planes, c) UV–vis absorption spectra, and d) PL spectra excited at 473 nm.

© 2020 WILEY-VCH Verlag GmbH & Co. KGaA, Weinheim

and similar to $MAPbI_3$ (794 nm). We also could observe the two more absorption peaks around 410 and 550 nm, which may correspond to two different interband transitions. Photoluminescence (PL) spectrum with 473 nm excitation is shown in Figure 1d where the PL peak is 785 nm. The whole data of SEM image, XRD spectrum, linear absorption, and PL spectrum of as-prepared (nonannealed) TCMHP film are presented in Figure S1 of the Supporting Information. To investigate the effect of nonperovskite δ-phase $FAPbI_3$ and PbI_2 on the optical properties of TCMHP perovskite, we have also performed XRD and UV–vis absorption spectroscopy of degraded TCMHP, which are shown in Figures S2 of the Supporting Information. It was confirmed from the UV–vis absorption spectra that the impurities are extremely small in the case of annealed TCMHP, which have not affected the optical properties of the perovskite. The detailed explanation was incorporated in the Supporting Information. The elemental composition of TCHMP phase, comprising Br Lα, Pb Mα, I Lα, and Cs Lα lines, has been confirmed using energy dispersive X-ray analysis, shown in Figure S3 of the Supporting Information.

Figure 2 shows the Stokes and anti-Stokes Raman spectra of TCMHP, recorded using micro-Raman spectrometer with an excitation wavelength of 785 nm and integration time of 1 s. As seen in Figure 2, there are two prominent Raman bands below 200 cm^{-1} observed at 86 and 143 cm^{-1}, which are similar with the longitudinal optical (LO) phonon modes of organic–inorganic lead halide perovskite, such as $MAPbBr_3$, $MAPbI_3$, $FAPbI_3$, etc.[41–43] Additionally, the other vibrational mode was also observed at 286 cm^{-1} and it could be related to organic cation vibrational frequency.

Inspired by the success of TCMHP films preparation could be made up of its conventional counter parts such as $FAPbI_3$, $MAPbBr_3$, and $CsPbI_3$.[44] Therefore, the observed vibrational modes in the Raman spectra of TCMHP could be confirmed as LO phonon modes. Moreover, the anti-Stokes spectra in Figure 2 illustrates that the phonon mode at −146 cm^{-1} (LO) is clearly exhibited but other phonon modes are not observed. However, the anti-Stokes Raman modes are observed to be very weak at room temperature in the case of hydride perovskites.[45] The observation of anti-Stokes Raman modes specifies the production of LO phonons in the material by the relaxation of excited electrons at the resonance condition.[46] At higher laser intensities, photoexcited electrons can occupy higher states by the absorption of photons and strongly couple with LO phonons through the Frohlich interaction.[47] In the hybrid perovskites, the selection of organic cation and halide composition has an impact on the Frohlich interaction or Frohlich electron–phonon coupling.[47] Particularly, bromide contained perovskites possess strong Frohlich electron–LO phonon coupling than in the case of iodide contained perovskites due to their minimal dielectric constant values at higher frequencies.[47]

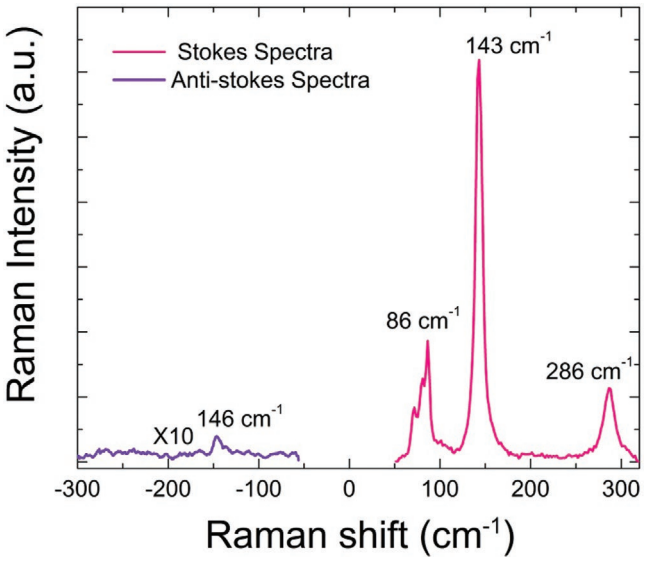

Figure 2. Raman spectra of TCMHP film, recorded using 785 nm wavelength. Stokes Raman spectra (pink color) and anti-Stokes Raman spectra (violet color) are shown in the spectra.

According to the previous report,[46] we tried to measure the phonon energy from the Raman spectra in Figure 2 by following the reported equation

$$\frac{I_{AS}}{I_S} \approx \frac{N_{LO}}{N_{LO}+1} \tag{1}$$

where I_{AS} and I_S are the anti-Stokes and Stokes intensities for a phonon mode in the Raman spectra, respectively. N_{LO} is the phonon occupation number, as given by the Bose–Einstein distribution, $N_{LO} = 1/\left[\exp\left(\hbar\omega_{LO}/K_BT\right)-1\right]$ and here, $\hbar$ is the Planck constant, ω_{LO} is the frequency of the LO mode, K_B is Boltzmann constant, and T is the temperature.

From the above two equations, the final equation is written as

$$\frac{I_S}{I_{AS}} \sim \exp\left(\hbar\omega_{LO}/K_BT\right) \tag{2}$$

The phonon energy ($\hbar\omega_{LO}$) calculated for the LO phonon mode of TCMHP was ≈67 meV at room temperature. Although, we cannot confirm all the aspects of LO phonons, such as the phonon modes and phonon energies of (TCMHP) new material from the Raman spectra, it does provide a limited information to understand the phonon modes and electron–LO phonon coupling. For clear understanding of phonon modes, phonon energy, and Raman spectra, further density functional theory calculations need to be performed.

Additionally, there are some reports which demonstrated that Frohlich electron–LO phonon coupling is the major reason of photoluminescence (PL) spectral broadening in hybrid perovskites at room temperature.[47,48] Baranowski et al.[48] have recently reported the temperature dependent PL studies of similar TCMHP perovskite $Cs_{0.05}MA_{0.16}FA_{0.79}Pb(I_{0.83}B_{r0.17})_3$ and demonstrated that increasing of PL spectra broadening (FWHM), ranging from ≈30 to ≈50 meV with respect to the temperature of 60–120 K. In our case, the FWHM of PL spectra for TCMHP $(Cs_{0.06}FA_{0.79}MA_{0.15})Pb(I_{0.85}Br_{0.15})_3$ is reached to ≈140 meV at room temperature (300 K). We believe that the reason behind the large PL spectral width of TCMHP at room temperature (300 K) could be attributed to the strong Frohlich electron–LO phonon coupling.

© 2020 WILEY-VCH Verlag GmbH & Co. KGaA, Weinheim

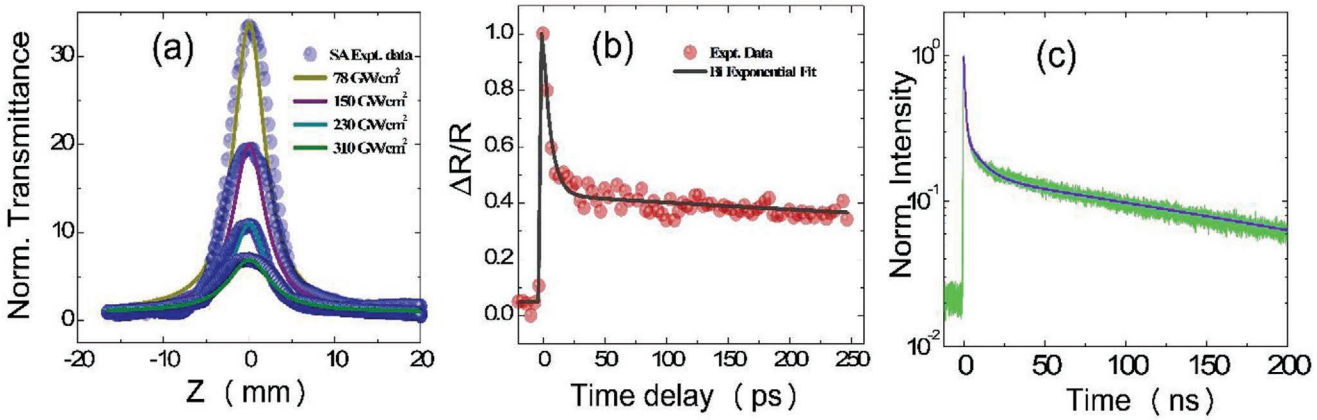

Figure 3. a) Open aperture Z-scan data of TCMHP film, obtained at the excitation wavelengths of 395 nm for 78, 150, 230, and 310 GW cm^{-2}. Solid spheres (light blue to dark blue color) are experimental results and colored curves are theoretical fits. b) Carrier dynamics of TCMHP film recorded by transient absorption spectroscopy with 220 μJ cm^{-2} pump fluence. Pump and probe wavelengths are 395 and 790 nm, respectively. Light gray solid curve is biexponential fit. c) Time-resolved photoluminescence decays of the TCMHP film with excitation at 480 nm and a fluence of 0.6 μJ cm^{-2}. Purple solid curve is biexponential fit. Time constants were extracted to be 7.56 and 202 ns.

To explore the NLO properties of TCHMP film, we performed Z-scan measurements at 395, 790, and 1200 nm. Experimental details are described in the Supporting Information. **Figure 3**a illustrates the open aperture (OA) Z-scan transmittance curves obtained at 395 nm for several intensities. We can see the transmittance peak at $Z = 0$ with symmetric edges, indicating that TCMHP film shows pure SA behavior at 395 nm. We note that exceptionally high optical transmittance ratio (≈32) is consistent with previous reports on saturable absorption showing high optical transmittance for other materials.[10,49] The curves were fitted by the intensity dependent nonlinear absorption equation, $\alpha(I) = \alpha_0 + \beta_{\text{eff}} I$, where β_{eff} is effective (negative) nonlinear absorption coefficient and described in Equations (S1) and (S5) of the Supporting Information. We extracted β_{eff} and saturation intensity (I_S) based on the relation given by $\beta_{\text{eff}} = -\alpha_0/I_S$. The obtained value of β_{eff} (I_S) are -1.0×10^{-4} cm W^{-1} (0.82 GW cm^{-2}), -2.8×10^{-5} cm W^{-1} (2.8 GW cm^{-2}), -1.0×10^{-5} cm W^{-1} (7.9 GW cm^{-2}), and -4.3×10^{-6} cm W^{-1} (18.1 GW cm^{-2}) at the peak intensities of 78, 150, 230, and 310 GW cm^{-2}, respectively. Interestingly, the normalized transmittance decreases with increasing peak intensity from 78 to 310 GW cm^{-2} when E (= 395 nm) > E_g (= 780 nm). In general, SA shows the increasing behavior of normalized optical transmittance with excitation intensity when $E > E_g$. The opposite behavior observed in TCHMP film could be due to the filling of trap states by the photoexcited electrons. [37] This process can be described as follows: first, electrons are photoexcited to the conduction band and some of electrons are trapped in the trap states. Subsequently, electrons in both the trap states and conduction band turn into thermal equilibrium through multiple trapping actions, resulting in recombination mediated by trap states in <1 ms time scale. Hence, available states in the conduction band can be increased with increasing the laser intensity, leading to lower normalized optical transmittance at higher intensity. The mechanism based on trap state is corroborated by carrier dynamics behavior. We performed the transient absorption (TA) (the Experimental Section) and time-resolved photoluminescence (TRPL) spectroscopies. In Figure 3b, we plotted the TA kinetics by measuring the normalized relative reflectance ($\Delta R/R$) with pump and probe pulses of 395 and 790 nm, respectively. The pump fluence was 220 μJ cm^{-2}. The TA data for lower pump fluences are presented in Figure S4a–c of the Supporting Information. The decay kinetics was fitted by biexponential decay function, leading to two decay time constants obtained with $\tau_1 = 6.3$ ps and $\tau_2 > 1$ ns. The τ_1 is associated with the rapid trapping and build-up of charge carriers process giving rise to filling the trap states and τ_2 corresponds to recombination process from trapped state to valance band. Since our time range is relatively shorter than fitted longer time constant value, we could not report the exact value of τ_2. To make it clearer, we also carried out TRPL experiments as shown in Figure 3c with excitation 480 nm and fluence of 0.6 μJ cm^{-2}. We note that very long decay time constant (≈200 ns) is attributed to the nonradiative recombination from trap state to valance band.[37]

There is possibly another mechanism for the decreasing SA transmittance observed at higher intensities. For any material with strong linear absorption (as is the case here with strong absorption at 400 nm), SA dominates at lower peak intensities. However, at higher intensities, the higher electronic states in the conduction band may be occupied further, which results in a lower transmittance in the OA Z-scan curve. For sufficiently large peak intensities (and below the damage threshold of the material), it could result in a complete RSA phenomenon or a combination of partial SA and partial RSA, which could be due to two step 2PA in the shorter pulse case and due to excited state absorption in the longer pulse case. Thus, the interplay between SA and RSA can lead to decreasing transmittance for increasing peak intensities, depending on the linear absorption coefficient and the peak intensity used.

In **Figure 4**a, Z-scan data of TCMHP film clearly exhibits RSA at 790 nm ($E \approx E_g$). The transmittance dip gets deeper with increasing input intensity. We analyzed this RSA phenomenon by plotting ln ($1-T_{OA}$) versus excitation intensity ln (I_0), confirming the 2PA at 35 GW cm^{-2} and 3PA from above 70 GW cm^{-2} (Figure S5, Supporting Information). The curves

© 2020 WILEY-VCH Verlag GmbH & Co. KGaA, Weinheim

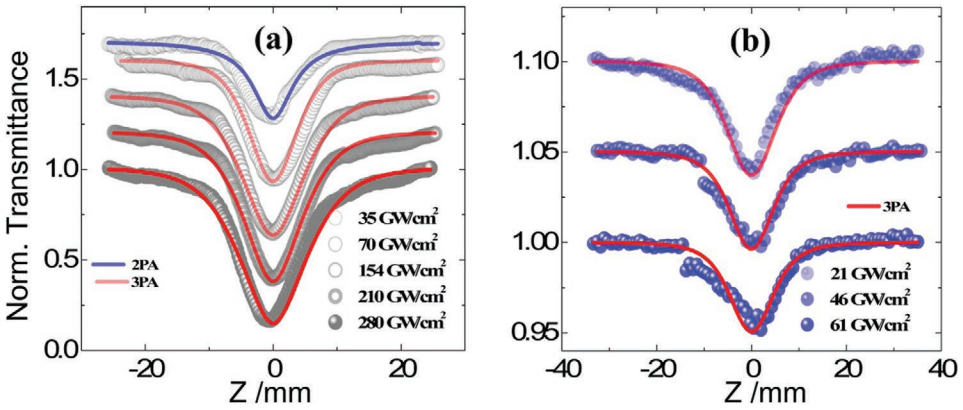

Figure 4. Open aperture Z-scan data of TCMHP film, obtained at the excitation wavelengths of a) 790 nm and b) 1200 nm for different intensities. a) Colored spheres (minimum to maximum) are experimental data and colored lines (blue – 2PA and red – 3PA) are theoretical fits and b) spheres (light blue to dark blue) are experimental data and solid color (red – 3PA) lines are theoretical fits.

were fitted with 2PA model for 35 GW cm^{-2} and 3PA model for above 70 GW cm^{-2} (Figure S5, Supporting Information), and the 2PA and 3PA coefficients can be estimated from the fitted curves in Figure 4a with Equations (S6) and (S7) of the Supporting Information, respectively. The obtained 2PA coefficient (β) is 2.10×10^{-6} cm W^{-1} at 35 GW cm^{-2}, and 3PA coefficients (γ) are 9.00×10^{2}, 6.99×10^{2}, 6.95×10^{2}, and 6.91×10^{2} cm^{3} GW^{-2} for peak intensities of 70, 154, 210, and 280 GW cm^{-2}, respectively.

Figure 4b presents the Z-scan transmittance traces of TCMHP film at 1200 nm, exhibiting RSA at different peak intensities. The traces were fitted with the corresponding theoretical equation of 3PA (Equation (S3), Supporting Information) and the γ values are estimated to be 26.5, 5.5, and 2.8 cm^{3} GW^{-2} for peak intensities of 21, 46, and 61 GW cm^{-2}, respectively.

The observed large nonlinearity and decreasing coefficient values as increasing excitation intensity could be attributed to high exciton density and resonance effects. Indeed, RSA response appeared at $E \approx E_g$ cannot be supported by MPA processes since they typically take place at $E < E_g$. Therefore, we need to explain this phenomenon explicitly.

To address the NLO responses shown in Figure 4a,b, we discussed the NLO phenomena based on the proposed schematic energy band diagram of TCHMP in **Figure 5** by following the previous reports,[50,51] where one lowest energy conduction band (CBM) and one highest energy valance band (VBM) exist as a function of k. It is worth noting that VBM → CBM is a major optical transition at R point corresponding to the bandgap (1.59 eV) of TCMHP. The shapes of VBM and CBM curvatures are more practical in reciprocal plane R to M, which could allow many optical transitions related to the obtained absorption continuum above the bandgap (absorption spectra in Figure 1c). Based on this, we describe nonlinear absorption behavior in Figure 5. 2PA phenomenon at 790 nm with relatively low intensity (thin red arrow) can occur through the transition from VBM to CBM near to M point. 3PA process at 1200 nm (purple arrow) can also take place through the transition from VBM to CBM near to M point. Regarding the 3PA at 790 nm with higher intensity (thick red arrow), we attributed this to phonon-assisted anti-Stokes processes,[52–54] provoked by electron–longitudinal optical (LO) phonon coupling in such a way that the photoexcited electrons may occupy the CBM with nonzero wavevector state through the simultaneous absorption of two photons and relax (dashed light black line) to the CBM with zero wavevector state leading to the creation of LO phonons. At higher intensity ($Z = 0$), photoexcited electrons near the bandgap jump into higher energy states of CBM by following the upconversion process through the resonant annihilation of LO phonons (green arrows). Hence, photoexcited electrons move to the higher energy states of CBM via the absorption of photons and resonant annihilation of LO phonons

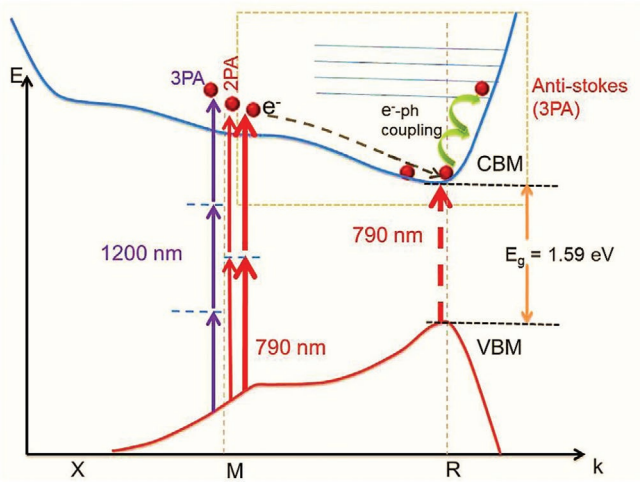

Figure 5. Schematic description of band structure of TCMHP is proposed based on the previous reports[50,51] and this simplified band diagram consists of one VBM and one CBM in TCMHP as a function of k vector. Major optical transition at R point (VBM → CBM) corresponds to the bandgap (1.59 eV) of TCMHP and the shape of VBM (blue color) and CBM (bark red color) curvatures are rough leading other possible optical transitions. Nonlinear absorption processes taking place in TCMH perovskite. Red and purple arrows correspond to 790 and 1200 nm, respectively. Thick/thick dashed and thin red arrows describe the relative intensity. Light black dashed line indicates the relaxation electron to the CBM edge and green line is effective CBM higher energy level (blue thin lines) resulting from phonon-assisted anti-Stokes processes due to the electron–LO phonon coupling.

© 2020 WILEY-VCH Verlag GmbH & Co. KGaA, Weinheim

leading to the phonon-assisted anti-Stokes process (RSA – 3PA, dark tan dashed box). We note that similar behavior has been reported in previous works. Tian et al. have recently demonstrated that the indirect bandgap semiconductor WSe_2 showed strong RSA behavior via phonon-assisted anti-Stokes process for $E \geq E_g$ (near the bandgap) in the femtosecond regime.[53] Zhang et al.[55] reported that cadmium sulphide nanoribbons, or nanobelts semiconductors with strong exciton–LO phonon coupling were exploited to accomplish the laser cooling

To compare the nonlinear optical properties of current TCMHP film with conventional organometal halide perovskite film, we performed the Z-scan measurement of $MAPbI_3$ film at 13, 27, 35, and 250 GW cm^{-2}. In **Figure 6**, we plotted the 2PA/3PA coefficients as a function of intensity for TCMHP and $MAPbI_3$ films at 790 nm.

Overall, the β values of TCMHP film are significantly higher than those of $MAPbI_3$ film and an order of magnitude higher near to the peak intensity of 35 GW cm^{-2}. While we could not observe the 3PA response for $MAPbI_3$ film, the obtained γ values of TCMHP film for each intensity are much larger than those of other perovskite film, micro-/nanocrystals, and single crystal.[15,16,56–60] The β and γ values of various types of perovskite materials reported in previous literatures and current study are summarized in **Table 1**. As observed in Table 1, a large variation exists in the nonlinear absorption coefficients extracted for the conventional perovskites in different morphology such as films, nanocrystals, and single crystals.

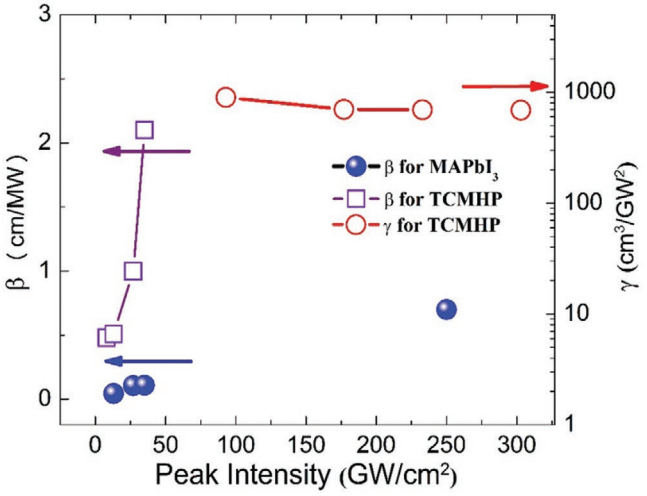

Figure 6. Intensity dependent nonlinear absorption coefficients of TCMH perovskite film and $MAPbI_3$ film, measured at the excitation wavelength of 790 nm. Blue sphere represents β for $MAPbI_3$ film, purple squares, and red color circles represent β and γ coefficients for TCMHP, respectively.

Table 1. Comparison the obtained 2PA/3PA coefficients of TCMHP with the conventional and other perovskites values in the literatures.

Material		Laser parameters/technique	NLO behavior and coefficients			Ref.
Name	Category		NLA coefficient		Nonlinear refractive index [cm^2 W^{-1}]	
			2PA [cm MW^{-1}]	3PA [cm^3 GW^{-2}]		
$CH_3NH_3PbI_3$	Film	40 fs, 800 nm, 1 kHz; Z-scan	$\beta = 0.7$			[23]
	Film	800 nm, 100 fs, 1 kHz	$\beta = -13.6$			[59]
	Film	200 fs, 1028 nm 1 kHz	$\beta_{eff} = 22$ to -0.04		$n_2 = 48$ to -0.24×10^{-12}	[58]
	Film	400 fs, 1028 nm, 1 kHz; Z-scan	$\beta = 272$			[24]
	Film	2.8 ps, 1560 nm, 20.1 MHz and 1.8 ps, 1930 nm, 32.3 MHz; Z-scan	$\beta = -360$ $\beta = -460$		$n_2 = 1.4 \times 10^{-8}$ $n_2 = 1.6 \times 10^{-8}$	[11] [11]
	Film	Z-scan; 40 ps, 1064 nm	$\beta = -2.25$		$n_2 = 3.7 \times 10^{-11}$	[10]
	Film	30 ns, 532 nm, 1 kHz; Z-scan	$\beta_{eff} = 22.2$ to -1620		$n_2 = -0.41$ to 34.4×10^{-9}	[58]
$CH_3NH_3PbBr_3$	Film	100 fs, 1 kHz, 800 nm and 1300 nm; random lasing experiment	2PA excitation RL threshold 0.75 mJ cm^{-2}	3PA excitation RL threshold 27 mJ cm^{-2}		[60]
	Film	40 fs, 800 nm, 1 kHz; Z-scan	$\beta = 0.05$		$n_2 = 7 \times 10^{-13}$	[23]
	Film	1 ns, 20 kHz, 1064 nm; Z-scan		$\gamma = 0$–300	$n_2 = 1.1$–3.5×10^{-9}	[27]
	Nanocrystals	Z-scan; 100 fs; 1240 nm; 1 kHz, Z-scan		$\gamma = 2.26 \times 10^{-5}$		[16]
$CH_3NH_3PbCl_3$	Film	40 fs, 800 nm, 1 kHz; Z-scan	$\beta = 0.015$		$n_2 = 3.4 \times 10^{-12}$	[23]
	Single crystal	30 ps; 1064 nm, 10 Hz; Z-scan		$\gamma = 0.05$		[15]
$CsPbBr_3$	Single crystal	30 ps, 1200 nm, 50 Hz; Z-scan		$\gamma = 0.14$		[56]
Cs_4PbBr_6	NCs Film	70 fs, 1 kHz, 500–1500 nm	$\beta \approx 0.1$	$\gamma = 0.065$–0.084		[57]
$(Cs_{0.06}FA_{0.79}MA_{0.15})Pb(I_{0.85}Br_{0.15})_3$	Film	50 fs, 1 kHz, 395 nm, 790 nm 1200 nm	$\beta = -100$ to -0.43 $\beta = 0.41$–2.1	$\gamma = 900$–691 $\gamma = 26.5$–2.8	$n_2 = -1 \times 10^{-11}$ $n_2 = -2.3 \times 10^{-11}$ $n_2 = 3.2 \times 10^{-11}$	Current work

© 2020 WILEY-VCH Verlag GmbH & Co. KGaA, Weinheim

However, a consensus seems to be emerging that 2PA coefficient or effective nonlinear absorption coefficient varies with different laser parameters and intrinsically, 3PA coefficient is not stated for conventional perovskites at resonant excitation wavelengths. Whereas the absorption of photons and resonant annihilation of LO phonons was found to support strong electron–LO phonon coupling in TCMHP at higher intensities leading to the phonon-assisted anti-Stokes process (RSA), which does affect the nonlinear absorption as strong 3PA process. TCMHP film with large 3PA coefficient could offer several significant advantages such as greater optical stabilization, improved sensitivity, large penetration depth, and better spatial confinement compare to the materials with 2PA in bioimaging and optical limiting applications. Moreover, TCMHP with 3PA can also be used in high power lasers to reduce the relative intensity noise, avoid the damage, and controlling spectral and spatial profiles, so it is crucial to understand the physical mechanism of two/three photon process in the materials for the development of new optical devices. Hence, our results that large 3PA process in TCMHP is obtained when excitation energy is near to the bandgap based on phonon-assisted anti-Stokes process are new findings in the field of perovskites.

Moreover, we have performed the nonlinear absorption studies of as-prepared TCMHP (standard or nonannealed) and degraded TCMHP samples to demonstrate the effect of those unwanted nonperovskite δ-phase $FAPbI_3$ and PbI_2 impurities on TCMHP, as shown in Figure S6 of the Supporting Information. This study also confirmed that the extremely small nonperovskite δ-phase $FAPbI_3$ and PbI_2 impurities have not affected the optical and NLO properties of TCMHP sample.

Figure 7 shows the closed aperture Z-scan normalized transmittance data of TCMHP film upon excitation at 395, 790, and 1200 nm. Self-defocusing behaviors were observed at 395 and 790 nm, while the self-focusing behavior at 1200 nm was recorded. The coefficients of nonlinear refractive index (n_2) retrieved from fitting using Equation (S8) of the Supporting Information are -1×10^{-11} cm^2 W^{-1} at 395 nm for 79 GW cm^{-2}, -2.34×10^{-11} cm^2 W^{-1} at 790 nm for 39 GW cm^{-2}, and 3.18×10^{-11} cm^2 W^{-1} at 1200 nm for 20 GW cm^{-2}. These values are an order of magnitude larger than those of organometal halide perovskite films with femtosecond laser pulse.[23,58]

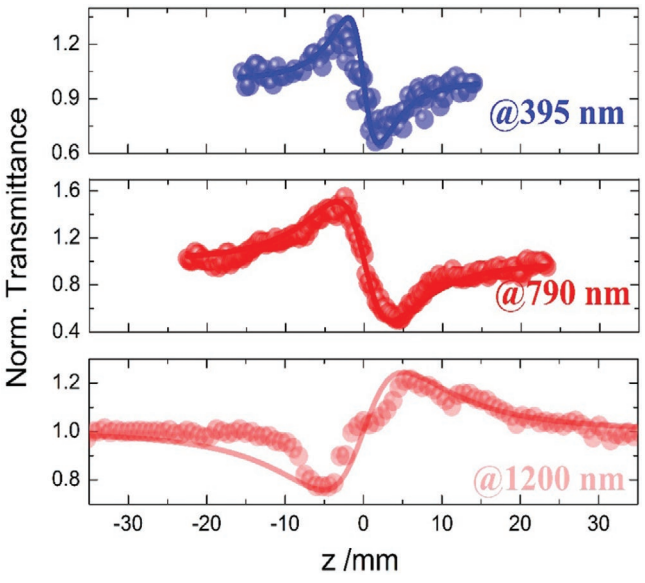

Figure 7. Closed aperture Z-scan data of TCMH perovskite film recorded at 395, 790, and 1200 nm. Color spheres (blue – 395 nm, red – 790 nm, and light red – 1200 nm) are experimental data and solid color lines (blue, red, and light red) are their respective theoretical fits.

Strong 2PA/3PA properties shown in TCMHP film can be manifested in the optical stabilization. To this end, we performed the optical stabilization measurements of TCMHP and $MAPbI_3$ films and compared them each other. **Figure 8** displays temporal fluctuations of femtosecond laser pulse intensity in the absence and presence of TCMHP film (Figure 8a), and $MAPbI_3$ film (Figure 8b), recorded for ≈100 s at 70 GW cm^{-2}. The data were recorded by a photodetector in combination with oscilloscope. TCMHP film exhibits less relative intensity fluctuations compared to $MAPbI_3$ film, indicating that strong 2PA/3PA effects of TCMHP film can lead to cutting down the noise. We observed that both samples show less intensity fluctuations compared with direct input laser noise without sample. We also estimated the relative intensity noise (RIN) in both cases as following equation

$$\mathrm{RIN} = \frac{V_{\max} - V_{\min}}{(V_{\max} + V_{\min})/2} \times 100\% \quad (3)$$

where $V_{\max}$ and $V_{\min}$ are the maximum and minimum intensities in the signal, respectively. The estimated RIN were 10.9%, 2.6%, and 4.3% for input laser beam without sample, TCMHP, and $MAPbI_3$ film, respectively. This indicates that TCMHP film is capable to lower the noise and stabilize intensity of laser beam by 4.2 times, which is significantly higher than $MAPbI_3$ film (2.5 times) and, 1 cm long liquid crystal sample (2.2 times).[61] Although Wei et al.[26] have reported the seven times improved optical stabilization property of $MAPbBr_3$ single crystal, it is worth noting that the thickness of TCMHP film we used (500 nm) is much thinner than theirs (3.8 mm).

3. Conclusion

In conclusion, we have investigated nonlinear optical response and photonic applications of TCMHP, $(Cs_{0.06}FA_{0.79}MA_{0.15})Pb(I_{0.85}Br_{0.15})_3$, film by performing Z-scan, carrier dynamics, time-resolved photoluminescence, and optical stabilization measurements. We observed the saturable absorption response at 395 nm ($>E_g$) and found that normalized transmittance decreases as excitation intensity increases, which is ascribed to the recombination of carriers mediated by trap states. Strong 3PA process at 790 nm ($\approx E_g$) was observed and attributed to the electrons–LO phonons coupling. A giant 3PA coefficient was obtained with a magnitude of ≈900 cm^3 GW^{-2} at 790 nm, which is superior to other conventional organometal halide perovskites films reported recently. We also demonstrated the effect of giant 2PA/3PA of TCMHP film on optical stabilization. The observed giant nonlinear absorption coefficients of

© 2020 WILEY-VCH Verlag GmbH & Co. KGaA, Weinheim

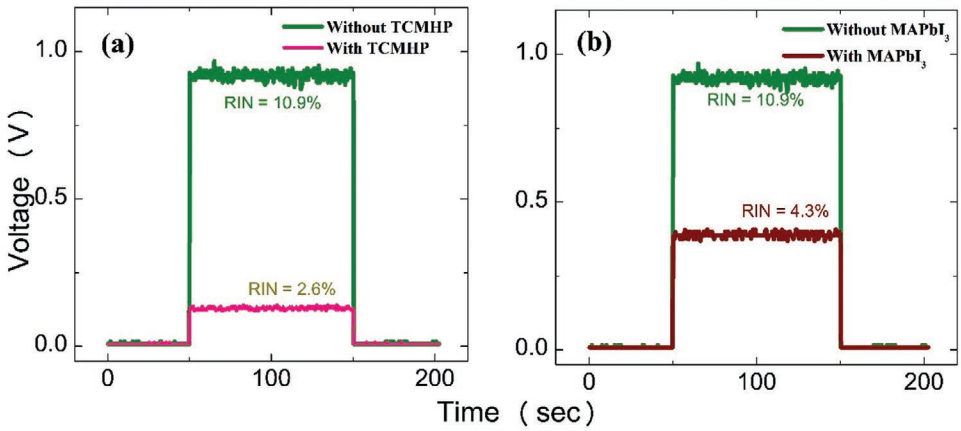

Figure 8. Optical stabilization measurement of femtosecond laser pulse. Intensity fluctuation of the input (olive curve) and output (pink – TCMHP and wine – $MAPbI_3$) of femtosecond laser pulses passed through the a) TCMHP film and b) $MAPbI_3$ film.

TCMHP film will greatly help in the development of a range of optoelectronic devices.

4. Experimental Section

Triple Cation Halide Mixed $(Cs_{0.06}FA_{0.79}MA_{0.15})Pb(I_{0.85}Br_{0.15})_3$ Perovskite Synthesis: The $(Cs_{0.06}FA_{0.79}MA_{0.15})Pb(I_{0.85}Br_{0.15})_3$ perovskite film was synthesized by using the reported two step and antisolvent method.[37] In this method, precursor solution of PbI_2 (1.2 M), FAI (1.11 M), MABr (0.21 M), and $PbBr_2$ (0.21 M) was prepared in a mixer of DMF:DMSO (4:1 volume ratio, v:v) followed by addition of 5 vol% from CsI stock solution (1.5 M in DMSO) and then filtered using a polytetrafluoroethylene membrane filter (0.2 µm pore size) to produce $(Cs_{0.06}FA_{0.79}MA_{0.15})Pb(I_{0.85}Br_{0.15})_3$ precursor solution. This precursor solution was spin-coated on the glass slide using two step program at 2000 and 6000 rpm for 10 and 30 s, respectively. After a particular time, another solvent chlorobenzene of 190 µL was added to the substrate for 30 s during the spinning. Subsequently, substrate was thermally annealed at 100 °C for 1 h and it was preserved in nitrogen filled glove box.

Z-Scan: In the case of 395 and 790 nm, femtosecond Ti:sapphire regenerative amplifier laser (Spectra-Physics, Spitfire ACE-35F-2KXP, Maitai SP) with pulse duration of 40 fs at a repetition rate of 1 kHz and a wavelength of 790 nm, was generated 395 nm wavelength by pumping to second harmonic crystal (SHG-BBO). The wavelength 790 nm was taken directly from the laser. The estimated pulse width of laser near to the sample was ≈50 fs. The wavelength 1200 nm was chosen from optical parametric amplifier (OPA-TOPAS-C, Light Conversion, Coherent) and it operates at 1 kHz repetition rate with tunable wavelengths (200–2400 nm). The average power of the pulse (≈50 fs) was about 150 mW. This OPA was pumped by the output of Ti:sapphire amplifier system (LIBRA, Coherent, ≈50 fs, 800 nm, 1 kHz, 2.5 W).

In the both cases, the pulse train from laser source was directed to the Brewster polarizer and half wave plate combination and this combination was used to control input power to the sample. The laser beam was focused on the perovskite film sample through the focusing lens of 200 mm by following the careful alignment. The sample was placed on 100 nm resolution translation stage and scanned along the Z-axis though collecting the transmitted data using the combination of computer controlled photodiode and lock-in-amplifier. The estimated beam waist diameter was ≈17, ≈25, and ≈54 µm and the corresponding Raleigh range of 2.2, ≈2.5 mm, and ≈7.8 mm for 395, 790, and 1200 nm, respectively. Nonlinear absorption studies were performed by open aperture Z-scan technique at different peak intensities to completely figure out the intensity dependent nonlinear absorption. Nonlinear refraction studies were also executed using closed aperture Z-scan technique at lower peak intensity to avoid the higher order nonlinear effects (the estimated value nonlinear phase change $\Delta\phi < \pi$).

Pump–Probe Experiments: Pump–probe spectroscopy was carried out using a chirped pulse amplified (CPA) Ti:sapphire laser system (Spectra-Physics, Spitfire ACE-35F-2KXP, Maitai SP) delivering nearly transform limited laser pulses (≈50 fs, 1 kHz repetition rate) at 790 nm wavelength of 5 W. 30 mW laser power was used in the experiments. The laser pulse spits into two pulse trains using 80/20 beam splitter to furnish pump and probe sources. A pump wavelength 395 nm was generated from second harmonic crystal (BBO). The delay line on the translation stage was inserted in one of the two beams, which is called as probe beam and the wavelength of probe is 790 nm. Pump and probe pulses pass through the separate lenses and focusing on sample. The estimated spot diameters on the sample to be 100 and 500 µm for pump and probe beams, respectively. The spatial overlap of the two pulses was aligned on the sample with the help of CCD camera, which can identify the positions of pump and probe spots. The ratio of pump was strictly followed to probe intensities to be >20%. A chopper was utilized to modulate the pump beam at 533 Hz and the differential probe reflectance from the sample was recorded by fast photodiode. The translation stage and fast photodiode were interfaced using Labview software. Autocorrelation technique was utilized for the optimizing experimental setup for getting the zero delay, which provided the spatial and temporal overlap of the beams meeting at the sample.

Supporting Information

Supporting Information is available from the Wiley Online Library or from the author.

Acknowledgements

This research was supported by the National Natural Science Foundation of China (Grant Nos. 91750205 and 11674178), Jilin Provincial Science & Technology Development Project (Grant No. 20180414019GH), K. C. Wong Education Foundation (GJTD-2018-08), and Strategic Priority Research Program of Chinese Academy of Sciences (No. XDA22010302).

Conflict of Interest

The authors declare no conflict of interest.

© 2020 WILEY-VCH Verlag GmbH & Co. KGaA, Weinheim

Keywords

anti-Stokes process, nonlinear optical properties, perovskite films, three-photon absorption, triple-cation mixed halide perovskites

Received: October 22, 2019
Revised: December 13, 2019
Published online: February 20, 2020

[1] W. S. Yang, J. H. Noh, N. J. Jeon, Y. C. Kim, S. Ryu, J. Seo, S. I. Seok, *Science* **2015**, *348*, 1234.
[2] A. Kojima, K. Teshima, Y. Shirai, T. Miyasaka, *J. Am. Chem. Soc.* **2009**, *131*, 6050.
[3] X. Li, D. Bi, C. Yi, J.-D. Décoppet, J. Luo, S. M. Zakeeruddin, A. Hagfeldt, M. A. Grätzel, *Science* **2016**, *353*, 58.
[4] Z.-K. Tan, R. S. Moghaddam, M. L. Lai, P. Docampo, R. Higler, F. Deschler, M. Price, A. Sadhanala, L. M. Pazos, D. Credgington, F. Hanusch, T. Bein, H. J. Snaith, R. H. Friend, *Nat. Nanotechnol.* **2014**, *9*, 687.
[5] Y.-H. Kim, H. Cho, J. H. Heo, T.-S. Kim, N. Myoung, C.-L. Lee, S. H. Im, T.-W. Lee, *Adv. Mater.* **2015**, *27*, 1248.
[6] K. Domanski, W. Tress, T. Moehl, M. Saliba, M. K. Nazeeruddin, M. Grätzel, *Adv. Funct. Mater.* **2015**, *25*, 6936.
[7] L. Su, Z. X. Zhao, H. Y. Li, J. Yuan, Z. L. Wang, G. Z. Cao, G. Zhu, *ACS Nano* **2015**, *9*, 11310.
[8] G. Xing, N. Mathews, S. S. Lim, N. Yantara, X. Liu, D. Sabba, M. Gratzel, S. Mhaisalkar, T. C. Sum, *Nat. Mater.* **2014**, *13*, 476.
[9] M. Saliba, S. M. Wood, J. B. Patel, P. K. Nayak, J. Huang, J. A. Alexander-Webber, B. Wenger, S. D. Stranks, M. T. Horantner, J. T. Wang, R. J. Nicholas, L. M. Herz, M. B. Johnston, S. M. Morris, H. J. Snaith, M. K. Riede, *Adv. Mater.* **2016**, *28*, 923.
[10] R. Zhang, J. Fan, X. Zhang, H. Yu, H. Zhang, Y. Mai, T. Xu, J. Wang, H. J. Snaith, *ACS Photonics* **2016**, *3*, 371.
[11] J. Yi, L. Miao, J. Li, W. Hu, C. Zhao, S. Wen, *Opt. Mater. Express* **2017**, *7*, 3894.
[12] F. O. Saouma, C. C. Stoumpos, J. Wong, M. G. Kanatzidis, J. I. Jang, *Nat. Commun.* **2017**, *8*, 742.
[13] W. Chen, S. Bhaumik, S. A. Veldhuis, G. Xing, Q. Xu, M. Gratzel, S. Mhaisalkar, N. Mathews, T. C. Sum, *Nat. Commun.* **2017**, *8*, 15198.
[14] G. Walters, B. R. Sutherland, S. Hoogland, D. Shi, R. Comin, D. P. Sellan, O. M. Bakr, E. H. Sargent, *ACS Nano* **2015**, *9*, 9340.
[15] F. O. Saouma, D. Y. Park, S. H. Kim, M. S. Jeong, J. I. Jang, *Chem. Mater.* **2017**, *29*, 6876.
[16] Y. Gao, S. Wang, C. Huang, N. Yi, K. Wang, S. Xiao, Q. Song, *Sci. Rep.* **2017**, *7*, 45391.
[17] W. Denk, J. Strickler, W. Webb, *Science* **1990**, *248*, 73.
[18] N. G. Horton, K. Wang, D. Kobat, C. G. Clark, F.W. Wise, C. B. Schaffer, C. Xu, *Nat. Photonics* **2013**, *7*, 205.
[19] J. E. Ehrlich, X. L. Wu, I.-Y. S. Lee, Z.-Y. Hu, H. Rockel, S. R. Marder, J. W. Perry, *Opt. Lett.* **1997**, *22*,1843.
[20] S. J. K. Pond, O. Tsutsumi, M. Rumi, O. Kwon, E. Zojer, J.-L. Bredas, S. R. Marder, J. W. Perry, *J. Am. Chem. Soc.* **2004**, *126*, 9291.
[21] B. H. Cumpston, S. P. Ananthavel, S. Barlow, D. L. Dyer, J. E. Ehrlich, L. L. Erskine, A. A. Heikal, S. M. Kuebler, I.-Y. Sandy Lee, D. McCord-Maughon, J. Qin, H. Rockel, M. Rumi, X.-L. Wu, S. R. Marder, J. W. Perry, *Nature* **1999**, *398*, 51.
[22] W.-G. Lu, C. Chen, D. Han, L. Yao, J. Han, H. Zhong, Y. Wang, *Adv. Opt. Mater.* **2016**, *4*, 1732.
[23] R. A. Ganeev, K. S. Rao, Z. Yu, W. Yu, C. Yao, Y. Fu, K. Zhang, C. Guo, *Opt. Mater. Express* **2018**, *8*, 1472.
[24] Y. Xie, J. Fan, C. Liu, S. Chi, Z. Wang, H. Yu, H. Zhang, Y. Mai, J. Wang, *Adv. Opt. Mater.* **2018**, *6*, 1700819.
[25] J. C. Johnson, Z. Li, P. F. Ndione, K. Zhu, *J. Mater. Chem. C* **2016**, *4*, 4847.
[26] T.-C. Wei, S. Mokkapati, T.-Y. Li, C.-H. Lin, G.-R. Lin, C. Jagadish, J.-H. He, *Adv. Funct. Mater.* **2018**, *28*, 1707175.
[27] I. Suárez, M. Vallés-Pelarda, A. F. Gualdrón-Reyes, I. Mora-Seró, A. Ferrando, H. Michinel, J. R. Salgueiro, J. P. Martínez Pastor, *APL Mater.* **2019**, *7*, 041106.
[28] K. N. Krishnakanth, S. Seth, A. Samanta, S. V. Rao, *Opt. Lett.* **2018**, *43*, 603.
[29] N. Pellet, P. Gao, G. Gregori, T. Y. Yang, M. K. Nazeeruddin, J. Maier, M. Gratzel, *Angew. Chem., Int. Ed.* **2014**, *53*, 3151.
[30] J. W. Lee, D. J. Seol, A. N. Cho, N. G. Park, *Adv. Mater.* **2014**, *26*, 4991.
[31] N. J. Jeon, J. H. Noh, W. S. Yang, Y. C. Kim, S. Ryu, J. Seo, S. I. Seok, *Nature* **2015**, *517*, 476.
[32] H. Choi, J. Jeong, H. B. Kim, S. Kim, B. Walker, G. H. Kim, J. Y. Kim, *Nano Energy* **2014**, *7*, 80.
[33] J. W. Lee, D. H. Kim, H. S. Kim, S. W. Seo, S. M. Cho, N. G. Park, *Adv. Energy Mater.* **2015**, *5*, 1501310.
[34] C. Yi, J. Luo, S. Meloni, A. Boziki, N. Ashari-Astani, C. Grätzel, S. M. Zakeeruddin, U. Röthlisberger, M. Grätzel, *Energy Environ. Sci.* **2016**, *9*, 656.
[35] M. Saliba, S. Orlandi, T. Matsui, S. Aghazada, M. Cavazzini, J.-P. Correa-Baena, P. Gao, R. Scopelliti, E. Mosconi, K.-H. Dahmen, F. De Angelis, A. Abate, A. Hagfeldt, G. Pozzi, M. Graetzel, M. K. Nazeeruddin, *Nat. Energy* **2016**, *1*, 15017.
[36] M. Saliba, T. Matsui, J. Y. Seo, K. Domanski, J. P. Correa-Baena, M. K. Nazeeruddin, S. M. Zakeeruddin, W. Tress, A. Abate, A. Hagfeldt, M. Gratzel, *Energy Environ. Sci.* **2016**, *9*, 1989.
[37] M. Abdi-Jalebi, Z. Andaji-Garmaroudi, S. Cacovich, C. Stavrakas, B. Philippe, J. M. Richter, M. Alsari, E. P. Booker, E. M. Hutter, A. J. Pearson, S. Lilliu, T. J. Savenije, H. Rensmo, G. Divitini, C. Ducati, R. H. Friend, S. D. Stranks, *Nature* **2018**, *555*, 497.
[38] F. Deschler, M. Price, S. Pathak, L. E. Klintberg, D. D. Jarausch, R. Higler, S. Huttner, T. Leijtens, S. D. Stranks, H. J. Snaith, M. Atature, R. T. Phillips, R. H. Friend, *J. Phys. Chem. Lett.* **2014**, *5*, 1421.
[39] M. Ahmadi, L. Collins, A. Puretzky, J. Zhang, J. K. Keum, W. Lu, I. Ivanov, S. V. Kalinin, B. Hu, *Adv. Mater.* **2018**, *30*, 1705298.
[40] J. Li, C. Ren, X. Qiu, X. Lin, R. Chen, C. Yin, T. He, *Photonics Res.* **2018**, *6*, 554.
[41] M. Nagai, T. Tomioka, M. Ashida, M. Hoyano, R. Akashi, Y. Yamada, T. Aharen, Y. Kanemitsu, *Phys. Rev. Lett.* **2018**, *121*, 145506.
[42] J. Yang, X. Wen, H. Xia, R. Sheng, Q. Ma, J. Kim, P. Tapping, T. Harada, T. W. Kee, F. Huang, Y.-B. Cheng, M. Green, A. Ho-Baillie, S. Huang, S. Shrestha, R. Patterson, G. Conibeer, *Nat. Commun.* **2017**, *8*, 14120.
[43] J. A. Steele, H. Yuan, C. Y. X. Tan, M. Keshavarz, C. Steuwe, M. B. J. Roeffaers, J. Hofkens, *ACS Nano* **2017**, *11*, 8072.
[44] T. Zhang, J. Wu, P. Zhang, W. Ahmad, Y. Wang, M. Alqahtani, H. Chen, C. Gao, Z. David Chen, Z. Wang, S Li, *Adv. Opt. Mater.* **2018**, *6*, 1701341.
[45] O. Yaffe, Y. Guo, L. Z. Tan, D. A. Egger, T. Hull, C. C. Stoumpos, F. Zheng, T. F. Heinz, L. Kronik, M. G. Kanatzidis, J. S. Owen, A. M. Rappe, M. A. Pimenta, L. E. Brus, *Phys. Rev. Lett* **2017**, *118*, 136001.
[46] X. B. Zhang, T. Taliercio, S. Kolliakos, P. Lefebvre, *J. Phys.: Condens. Matter* **2001**, *13*, 7053.
[47] A. D. Wright, C. Verdi, R. L. Milot, G. E. Eperon, M. A. Pérez-Osorio, H. J. Snaith, F. Giustino, M. B. Johnston, L. M. Herz, *Nat. Commun.* **2016**, *7*, 11755.
[48] M. Baranowski, J. M. Urban, N. Zhang, A. Surrente, D. K. Maude, Z Andaji-Garmaroudi, S. D. Stranks, P. Plochocka, *J. Phys. Chem. C* **2018**, *122*, 17473.

 © 2020 WILEY-VCH Verlag GmbH & Co. KGaA, Weinheim

[49] C. Zhao, H. Zhang, X. Qi, Y. Chen, Z. Wang, S. Wen, D. Tang, *Appl. Phys. Lett.* **2012**, *101*, 211106.
[50] L. M. Herz, *Annu. Rev. Phys. Chem.* **2016**, *67*, 65.
[51] I. Minda, J. Horn, E. Ahmed, D. Schlettwein, H. Schwoerer, *ChemPhysChem* **2018**, *19*, 3010.
[52] Q. Zhang, X. Liu, M. I. Utama, G. Xing, T. C. Sum, Q. Xiong, *Adv. Mater.* **2016**, *28*, 276.
[53] X. Tian, R. Wei, Q. Guo, Y. J. Zhao, J. Qiu, *Adv. Mater.* **2018**, *30*, 1801638.
[54] Y.-H. Qiu, K. Chen, S.-J. Ding, F. Nan, Y.-J. Lin, J.-X. Ma, Z.-H. Hao, L. Zhou, Q.-Q. Wang, *Nanoscale* **2019**, *11*, 8538.
[55] J. Zhang, D. Li, R. Chen, Q. Xiong, *Nature* **2013**, *493*, 504.
[56] D. J. Clark, C. C. Stoumpos, F. O. Saouma, M. G. Kanatzidis, J. I. Jang, *Phys. Rev. B* **2016**, *93*, 195202.
[57] K. N. Krishnakanth, S. Seth, A. Samanta, S. V. Rao, *Nanoscale* **2019**, *11*, 945.
[58] B. S. Kalanoor, L. Gouda, R. Gottesman, S. Tirosh, E. Haltzi, A. Zaban, Y. R. Tischler, *ACS Photonics* **2016**, *3*, 361.
[59] W. Liu, J. Xing, J. Zhao, X. Wen, K. Wang, P. Lu, Q. Xiong, *Adv. Opt. Mater.* **2017**, *5*, 1601045.
[60] G. Weng, J. Xue, J. Tian, X. Hu, X. Bao, H. Lin, S. Chen, Z. Zhu, J. Chu, *ACS Photonics* **2018**, *5*, 2951.
[61] G. S. He, T.-C. Lin, P. N. Prasad, C.-C. Cho, L.-J. Yu, *Appl. Phys. Lett.* **2003**, *82*, 4717.

© 2020 WILEY-VCH Verlag GmbH & Co. KGaA, Weinheim